

H I absorption at $z \sim 0.7$ against the lobe of the powerful radio galaxy PKS 0409–75

Elizabeth K. Mahony^{1,2*}, James R. Allison^{3,2}, Elaine M. Sadler^{1,2,4}, Sara L. Ellison⁵, Sui Ann Mao⁶, Raffaella Morganti^{7,8}, Vanessa A. Moss^{1,4}, Amit Seta⁹, Clive N. Tadhunter¹⁰, Simon Weng^{1,4}, Matthew T. Whiting¹, Hyein Yoon^{2,4}, Martin Bell¹¹, John D. Bunton¹, Lisa Harvey-Smith^{12,13}, Amy Kimball¹⁴, Bärbel S. Koribalski^{1,13} and Max A. Voronkov¹

¹Australia Telescope National Facility, CSIRO Space and Astronomy, PO Box 76, Epping, NSW 1710, Australia.

²ARC Centre of Excellence for All-Sky Astrophysics in 3 Dimensions (ASTRO 3D)

³Sub-Dept. of Astrophysics, Department of Physics, University of Oxford, Denys Wilkinson Building, Keble Rd., Oxford, OX1 3RH, UK

⁴Sydney Institute for Astronomy, School of Physics A28, The University of Sydney, NSW 2006, Australia.

⁵Department of Physics & Astronomy, University of Victoria, Finnerty Road, Victoria, British Columbia, V8P 1A1, Canada

⁶Max Planck Institute for Radio Astronomy, Auf dem Hügel 69, 53121 Bonn, Germany

⁷ASTRON, the Netherlands Institute for Radio Astronomy, Postbus 2, 7990 AA, Dwingeloo, The Netherlands.

⁸Kapteyn Astronomical Institute, University of Groningen, Postbus 800, 9700 AV Groningen, The Netherlands.

⁹Research School of Astronomy & Astrophysics, The Australian National University, Canberra ACT 2611, Australia

¹⁰Department of Physics & Astronomy, University of Sheffield, Sheffield S3 7RH.

¹¹University of Technology Sydney, 15 Broadway, Ultimo NSW 2007, Australia.

¹²School of Physics, University of New South Wales, Sydney, NSW 2052, Australia.

¹³School of Computer, Data and Mathematical Sciences, Western Sydney University, Locked Bag 1797, Penrith, NSW, 2751, Australia.

¹⁴National Radio Astronomy Observatory, 1003 Lopezville Rd., Socorro, NM, 87801, USA.

Accepted XXX. Received YYY; in original form ZZZ

ABSTRACT

We present results from a search for the H I 21-cm line in absorption towards 16 bright radio sources with the 6-antenna commissioning array of the Australian Square Kilometre Array Pathfinder (ASKAP). Our targets were selected from the 2-Jy sample, a flux-limited survey of the southern radio sky with extensive multi-wavelength follow-up. Two sources were detected in H I absorption including a new detection towards the bright FR II radio galaxy PKS 0409–75 at a redshift of $z = 0.674$. The H I absorption line is blueshifted by ~ 3300 km s⁻¹ compared to the optical redshift of the host galaxy of PKS 0409–75 at $z = 0.693$. Deep optical imaging and spectroscopic follow-up with the GMOS instrument on the Gemini-South telescope reveal that the H I absorption is associated with a galaxy in front of the southern radio lobe with a stellar mass of $3.2 - 6.8 \times 10^{11} M_{\odot}$, a star-formation rate of $\sim 1.24 M_{\odot} \text{ yr}^{-1}$ and an estimated H I column density of $2.16 \times 10^{21} \text{ cm}^{-2}$, assuming a spin temperature of $T_{\text{spin}} = 500$ K and source covering factor of $C_f = 0.3$. Using polarisation measurements of PKS 0409–75 from the literature we estimate the magnetic field of the absorbing galaxy to be $\sim 14.5 \mu\text{G}$, consistent with field strengths observed in nearby spiral galaxies, but larger than expected for an elliptical galaxy. Results from this pilot study can inform future surveys as new wide-field telescopes allow us to search for 21-cm H I absorption towards all bright radio sources as opposed to smaller targeted samples.

Key words: galaxies: active – galaxies: ISM – galaxies: individual (PKS 0409–75) – radio lines: galaxies

1 INTRODUCTION

It is well established that the brightest extragalactic radio sources are produced by synchrotron-emitting radio jets launched from a central active galactic nucleus (AGN; Condon 1989; Condon et al.

* E-mail: elizabeth.mahony@csiro.au

1998; Mauch & Sadler 2007; Condon et al. 2019). The precise conditions required to trigger and form these jets remains an active area of research, but the presence of cold gas as a source of fuel for the central AGN is a critical component. As such, studying the distribution and kinematics of cold gas at the cores of active galaxies is crucial to understanding the fuelling and feedback processes that shape their evolution. Observing the dynamics and kinematics of the gas can provide some of the most direct evidence for fuelling (Maccagni et al. 2014; Tremblay et al. 2016; Chandola et al. 2020) and feedback processes (Morganti et al. 2005; Dasyra & Combes 2012; Morganti et al. 2013; Tadhunter et al. 2014; Oosterloo et al. 2019; Herrera-Camus et al. 2020; Schulz et al. 2021) in AGN.

Searching for H I 21-cm absorption against bright radio sources is a highly effective tool in probing the dynamics of the cool, neutral gas, particularly beyond the nearby Universe ($z > 0.2$) where emission line studies require prohibitively long integration times (see Morganti et al. 2015; Morganti & Oosterloo 2018 and references therein). In addition to being detectable out to large redshift, 21-cm absorption line studies have the advantage of directly tracing the gas at the position of the radio AGN, are more sensitive to the colder gas, and have the potential to probe gas at higher spatial resolution (e.g. Beswick et al. 2002, 2004; Morganti et al. 2013; Schulz et al. 2018).

van Gorkom et al. (1989) carried out one of the first systematic searches for H I absorption in radio-loud AGN with the Very Large Array (VLA), detecting H I in 13% of the 29 radio galaxies observed. Since then, there have been numerous studies searching for H I absorption using different source selections (Morganti et al. 2001; Gupta & Saikia 2006; Curran et al. 2008; Geréb et al. 2015; Allison et al. 2015; Maccagni et al. 2017; Murthy et al. 2021). These searches typically detect the presence of neutral gas in approximately 30% of sources (Geréb et al. 2015; Maccagni et al. 2017), although this varies significantly according to the sample selection. Numerous studies have reported higher detection rates in compact radio sources ranging from 32-57% (Vermeulen et al. 2003; Pihlstrom et al. 2003; Gupta & Saikia 2006; Chandola et al. 2013; Maccagni et al. 2017; Murthy et al. 2021) while a study of galaxy mergers found H I absorption in 84% of the sample (Dutta et al. 2018, 2019). By comparison, Maccagni et al. (2017) report a detection rate of $\sim 15\%$ for extended radio sources and Murthy et al. (2021) did not detect any H I 21-cm absorption lines towards the 14 resolved radio sources in their sample.

The majority of these studies have been carried out at low redshifts largely due to the available frequency coverage of most interferometers, such as the Westerbork Synthesis Radio Telescope (WSRT; Geréb et al. 2015; Maccagni et al. 2017; Vermeulen et al. 2003), the VLA (van Gorkom et al. 1989; Morganti et al. 2005; Murthy et al. 2021) and the Australia Telescope Compact Array (ATCA; Allison et al. 2012b; Glowacki et al. 2017). In addition, the relatively narrow bandwidths meant that prior knowledge of the redshift of the radio source was needed to ensure the H I 21-cm line was observable in the frequency range available. This was particularly true for observations carried out prior to significant upgrades of the ATCA and VLA which increased the available bandwidth from 2×128 MHz to 2×2048 MHz frequency windows for ATCA (Wilson et al. 2011) and from 100 MHz to 2–8 GHz (depending on the spectral resolution and frequency coverage) for the VLA (Perley et al. 2011). This requirement of prior knowledge of the spectroscopic redshift introduces various selection biases since the optical magnitude of the galaxy needs to be sufficiently bright to obtain a redshift measurement. An increasing number of high-redshift searches ($z > 1$) have been performed using the Giant

Metrewave Radio Telescope (GMRT; Curran et al. 2008; Curran et al. 2012; Aditya 2019; Aditya et al. 2021), significantly enhanced thanks to the recent upgrade which increased the instantaneous bandwidth from 32 MHz to 400 MHz and increasing the available frequency coverage from 50-1500 MHz (Aditya et al. 2016; Aditya 2019; Dutta et al. 2020).

The advent of new facilities with wider bandwidths, including the Australian Square Kilometre Array Pathfinder (ASKAP; Hotan et al. 2021), MeerKAT (Jonas & MeerKAT Team 2016), Westerbork Aperture Tile in Focus (AperTIF; Oosterloo et al. 2009) and the upgraded GMRT (Gupta et al. 2017), have opened up a much larger frequency window to search for H I in absorption. Importantly, the large instantaneous bandwidth (~ 300 MHz for ASKAP and AperTIF and ~ 400 MHz for uGMRT and MeerKAT), and relatively Radio Frequency Interference (RFI)-free spectrum allow us to search for absorption lines without prior knowledge of the redshift. This has been demonstrated by the recent detection of several H I absorption systems where the redshift of the background radio source was not known before the observations (Allison et al. 2015; Moss et al. 2017; Glowacki et al. 2019; Allison et al. 2020; Chowdhury et al. 2020; Sadler et al. 2020).

This paper presents a search for H I absorption towards 16 powerful radio galaxies with the Boolardy Engineering Telescope Array (BETA); the 6-element commissioning array of ASKAP (Hotan et al. 2014; McConnell et al. 2016). The sources were selected from the 2-Jy sample (Wall & Peacock 1985; Tadhunter et al. 1993) to ensure there was sufficient radio continuum to be able to detect H I absorption with the 6 antennas of ASKAP-BETA. Section 2 describes the sample selection, observations and data reduction of the ASKAP-BETA observations and Section 3 presents the results of the ASKAP-BETA search for H I absorption. Section 4 describes follow-up optical observations carried out with the Gemini-South telescope. We discuss the properties of the H I absorption detection and implications for similar detections in upcoming large absorption line surveys in Section 5 before concluding in Section 6.

2 RADIO OBSERVATIONS

2.1 Sample selection

A sample of 16 bright radio galaxies was selected from the 2-Jy sample (Wall & Peacock 1985); a complete, flux-density limited sample of sources brighter than 2 Jy at 2.7 GHz. An extensive campaign of multi-wavelength follow-up has been carried out for 2-Jy sources at declinations $\delta < +10^\circ$, steep spectral indices ($\alpha_{2.7}^{4.8} < -0.5$)¹ and redshifts between $0.05 < z < 0.7$ (Tadhunter et al. 1993). This includes high-resolution radio imaging (Morganti et al. 1999), deep optical imaging and spectroscopy (Ramos Almeida et al. 2011), mid and far-IR imaging (Dicken et al. 2008, 2012) and X-ray observations (Mingo et al. 2014). The completeness of the multi-wavelength follow-up make it an ideal sample to search for H I absorption as it is a radio-selected sample, yet has the accompanying multi-wavelength data needed to provide redshifts and luminosities without introducing additional selection effects based on the optical properties (e.g. such as those introduced by selecting sources with existing spectroscopic data from large optical surveys which can add an additional optical flux-limit). Only sources with redshifts $z > 0.2$

¹ where $S_\nu \propto \nu^\alpha$ and the sub/super-scripts refer to the frequency range in GHz between which the spectral index was measured

were included to ensure the H I line would fall in the frequency range observed which can trace the H I line from $0.2 < z < 1$.

A summary of the properties of these 16 radio galaxies is given in Table 1. All sources have been classified according to their radio morphology (Fanaroff-Riley Type I/II (FRI/FRII) or Compact Steep Spectrum (CSS) objects) and their optical spectral properties (Narrow or Broad Line Radio Galaxy (NLRG/BLRG, QSO) given in Tadhunter et al. (1993); Morganti et al. (1993). We also list the measured flux densities at 4.8 GHz (both the core and total flux measurements as given in Morganti et al. (1993)) and at 850 MHz from the Rapid ASKAP Continuum Survey (RACS; McConnell et al. 2020; Hale et al. 2021).

2.2 ASKAP-BETA

Observations were carried out using ASKAP-BETA over the period from November 2014 - February 2016. This 6-element interferometer had baselines ranging from 37 to 916m, leading to a synthesised beam of approximately 1.5 arcmin at 850 MHz when using natural weighting.

The majority of sources were observed over the frequency range 711.5 – 1015.5 MHz corresponding to H I redshifts in the range $0.4 < z < 1.0$. Five targets were observed at higher frequencies (967.5 – 1271.5 MHz) which covers the redshift range $0.2 < z < 0.4$, however, this frequency range is more strongly affected by RFI from satellites and aircraft, with approximately 30-50% of the data being flagged. Each target was placed at the phase centre of the central beam, with the remaining 8 beams arranged in a diamond footprint (see Allison et al. 2015 for more details). The primary flux calibrator, PKS B1934–638, was observed for short scans of 5–15 min in each beam at the beginning of each observing run. A summary of the ASKAP-BETA observations is given in Table A1.

The data were reduced using a custom-built MIRIAD pipeline as described in detail by Allison et al. (2015). In summary, the data were separated into 64 subbands corresponding to the 4-5 MHz beam-forming frequency intervals used by ASKAP-BETA and each subband then reduced independently using the standard flagging, calibration and imaging MIRIAD tasks. Processing each subband separately provided the advantage of allowing parallelisation of the data reduction, but also corrected for the discrete jumps in the gain solutions at the edge of the beam-forming intervals.

The continuum subtraction was performed in two steps: first, by subtracting the CLEAN components generated from a continuum image of each subband from the visibilities using UVMODEL, and then by fitting a second-order polynomial using UVLIN to subtract any residual flux from continuum sources that were not sufficiently removed from the visibilities. Finally, a spectrum was extracted at the peak flux density of the target source (which were all unresolved by ASKAP-BETA) at the full spectral resolution of 18.5 kHz which corresponds to a rest-frame velocity resolution of $5.5\text{--}7.8 \text{ km s}^{-1}$. For consistency, the data were re-reduced after the completion of all observations to ensure the same version of the pipeline was used for all targets.

After reducing each observation independently, the extracted spectrum for each target was averaged and weighted by the inverse-variance measured across the channel images. For more details on the data processing we refer the reader to Allison et al. (2015).

3 RESULTS

H I 21-cm absorption was detected in two of the sixteen targets observed with ASKAP; one associated with PKS 0023–26 at a redshift of $z = 0.322$ (Vermeulen et al. 2003) and a new detection towards PKS 0409–75 at a redshift of $z = 0.674$. The H I spectra are shown in Figure 1. Here we display a small fraction of the total bandwidth around the expected frequency of the H I 21-cm line determined from the optical redshift of the radio galaxy. An example of the full spectrum obtained from ASKAP-BETA is shown in B1. The primary aim of this work is to search for associated absorption, but the wide bandwidth provided by ASKAP-BETA also allows us to search for any intervening absorption along the line-of-sight. No other detections of H I 21-cm absorption were observed in this sample, but given the small sample size and amount of bandwidth flagged due to RFI at the lower frequencies this is not unexpected.

3.1 H I properties of the sample

While this paper presents a comparatively small sample of 16 targets that were searched for H I 21-cm absorption, a detection rate of 12.5% (2/16) may appear to be at the lower end of the range of previously reported detection rates for associated 21-cm absorption (Morganti et al. 2001; Vermeulen et al. 2003; Curran et al. 2008; Chandola et al. 2013; Geréb et al. 2015; Maccagni et al. 2017; Dutta et al. 2018; Murthy et al. 2021). However, a number of uncertainties make it difficult to confirm this and carry out a fair comparison with previous studies. The biggest factors contributing to this are: (1) the wide range in integration time (and therefore sensitivity reached) for objects in the sample as all observations were carried out in an opportunistic fashion during the commissioning period, and (2) the large range of radio continuum source structure of our sample. The latter leads to highly uncertain covering factors (C_f) which can change the optical depth and H I column density limits by orders of magnitude.

The covering factor is often estimated by using the ratio of core to total flux density ($\langle R \rangle$) which provides a measure of the compactness of the radio source, limited by the spatial resolution of the available data (see e.g. Kanekar et al. 2009a). For compact sources (i.e. such as those classified as CSS in Table 1) this gives a covering factor of $C_f = 1$ which is the typically assumed C_f for most 21 cm absorption line studies, driven by the fact that most samples are selected based on source compactness, or a minimum core flux density (e.g. Morganti et al. 2001; Maccagni et al. 2017). In addition, we also need to make an assumption about T_{spin} , the harmonic mean spin (excitation) temperature over the line-of-sight gas. At $z < 1$, the measured spin temperatures on sight lines through galaxies range from 100-1000 K (Kanekar et al. 2014; Allison 2021) so in the absence of a direct measurement for these sources we assume a spin temperature of $T_{\text{spin}} = 500 \text{ K}$. This value was chosen as the approximate mid-point of the range of observed T_{spin} , but could easily change the estimated N_{HI} by a factor of 2 if T_{spin} is similar to the Milky Way value of $\sim 300 \text{ K}$ (Dickey et al. 2009; Murray et al. 2018), or $\sim 1000 \text{ K}$ as observed in some damped Lyman- α systems (DLAs, e.g. Kanekar et al. 2009b; Kanekar et al. 2014) and in the central regions of AGN (Bahcall & Ekers 1969; Holt et al. 2006).

Having measured the absorption fraction ($\frac{\Delta S}{S_{\text{cont}}}$), and using these assumptions for C_f and T_{spin} we can calculate the optical depth (τ) and N_{HI} from the following equations:

$$\tau = -\ln \left(1 - \frac{\Delta S}{C_f S_{\text{cont}}} \right). \quad (1)$$

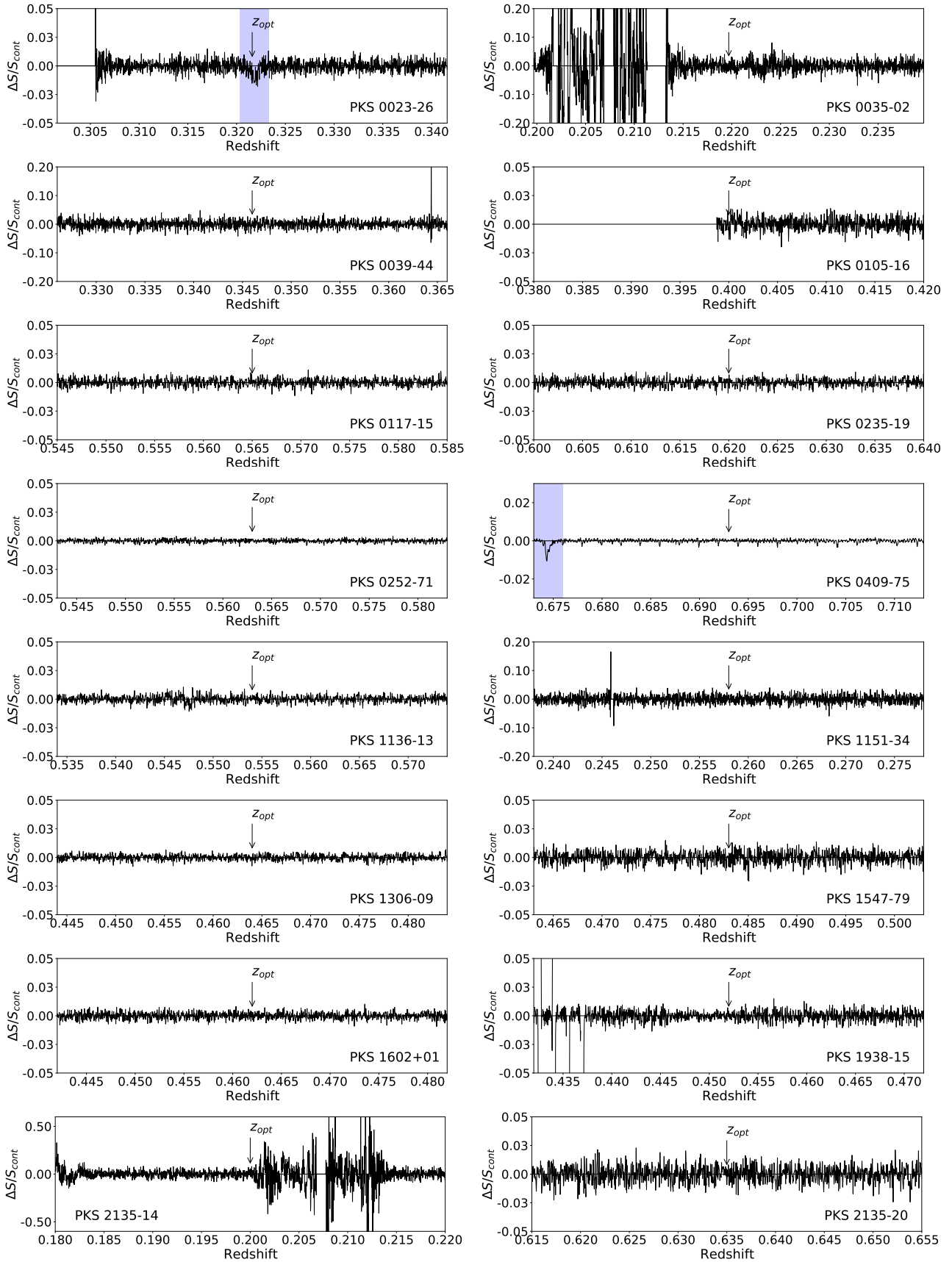


Figure 1. ASKAP-BETA spectra of 16 sources selected from the 2-Jy sample showing the fractional absorption (the measured flux density in absorption (ΔS) divided by the continuum flux density (S_{cont})) for a small range around the optical redshift of the host galaxy (marked by the arrow). H I 21-cm absorption is observed in PKS 0023–26 at $z = 0.322$ and PKS 0409–75 at $z = 0.674$, highlighted by the blue shaded boxes. Small artefacts can be seen in the spectrum of PKS 0409-75 corresponding to a channelisation error at the edges of the 1 MHz coarse channels. This issue was discovered during the ASKAP commissioning period and has since been corrected. The impact of RFI from aircraft and satellites is much greater at the higher frequencies (corresponding to $z_{\text{HI}} < 0.4$).

Table 1. Properties of the 2-Jy sources that were searched for H I absorption with ASKAP-BETA. The radio morphology class refers to either a Fanaroff-Riley Type I/II radio galaxy or a Compact Steep Spectrum Source (CSS) and are taken from [Morganti et al. \(1993\)](#), as are the total and core flux densities measured at 4.8 GHz. The optical classification is determined from the spectroscopic properties and defined as either a Quasi-Stellar Object (QSO), Narrow-line or Broad-line Radio Galaxy (NLRG/BLRG) as designated in [Tadhunter et al. \(1993\)](#). The final column lists the 850 MHz flux density from the Rapid ASKAP Continuum Survey (RACS). All flux densities are listed in Jy.

Source	RA (J2000)	DEC (J2000)	z	Radio cl.	Opt. cl.	$S_{\text{tot},4.8\text{ GHz}}$	$S_{\text{core},4.8\text{ GHz}}$	$S_{850\text{ MHz}}$
PKS 0023–26	00 ^h 25 ^m 49 ^s .16	–26°02′12″.6	0.322	CSS	NLRG	3.41	unresolved	11.6
PKS 0035–02	00 ^h 38 ^m 20 ^s .52	–02°07′40″.7	0.220	(FR II)*	BLRG	2.64	0.662	9.1
PKS 0039–44	00 ^h 42 ^m 08 ^s .98	–44°14′00″.5	0.346	FR II	NLRG	1.17 [†]	no core	5.7
PKS 0105–16	01 ^h 08 ^m 16 ^s .90	–16°04′20″.6	0.400	FR II	NLRG	1.17	<0.002	6.3
PKS 0117–15	01 ^h 20 ^m 27 ^s .10	–15°20′16″.6	0.565	FR II	NLRG	1.6	no core	7.1
PKS 0235–19	02 ^h 37 ^m 43 ^s .45	–19°32′33″.3	0.620	FR II	BLRG	1.44	<0.0002	6.8
PKS 0252–71	02 ^h 52 ^m 46 ^s .16	–71°04′35″.3	0.563	CSS	NLRG	1.58	unresolved	8.8
PKS 0409–75	04 ^h 08 ^m 48 ^s .49	–75°07′19″.3	0.693	FR II	NLRG	4.25	no core	19.6
PKS 1136–13	11 ^h 39 ^m 10 ^s .70	–13°50′43″.6	0.554	FR II	QSO	1.9	no core	6.2
PKS 1151–34	11 ^h 54 ^m 21 ^s .79	–35°05′29″.1	0.258	CSS	QSO	2.78	unresolved	7.6
PKS 1306–09	13 ^h 08 ^m 39 ^s .12	–09°50′32″.5	0.464	CSS	NLRG	1.9	unresolved	5.6
PKS 1547–79	15 ^h 55 ^m 21 ^s .65	–79°40′36″.3	0.483	FR II	BLRG	1.38	<0.003	6.1 [‡]
PKS 1602+01	16 ^h 04 ^m 45 ^s .32	+01°17′51″.0	0.462	FR II	BLRG	1.13	0.065	6.8
PKS 1938–15	19 ^h 41 ^m 15 ^s .07	–15°24′31″.3	0.452	FR II	BLRG	2.34	no core	9.2
PKS 2135–14	21 ^h 37 ^m 45 ^s .17	–14°32′55″.8	0.200	FR II	QSO	1.38	0.121	5.8
PKS 2135–20	21 ^h 37 ^m 50 ^s .01	–20°42′31″.6	0.635	CSS	BLRG	1.53	unresolved	5.2

* Brackets indicate an uncertain radio morphology for this object.

[†] Flux densities published in [Morganti et al. \(1999\)](#) for this object.

[‡] Flux density for this source was obtained from the initial RACS catalogue available from the CSIRO ASKAP Science Data Archive (CASDA)².

$$N_{\text{HI}} = 1.823 \times 10^{18} T_{\text{spin}} \int \tau dv. \quad (2)$$

In [Table 2](#) we calculate N_{HI} using both $C_f = 1$ and $C_f = R$ where this information was available. The core-total flux density ratios (R) were calculated from the higher resolution 4.8 GHz radio data observed with either the VLA or ATCA as given in [Table 1](#) ([Morganti et al. 1993](#)). Assuming a source covering factor of 1 is reasonable for compact radio sources, but is unphysical for extended radio sources with little core flux and will significantly underestimate N_{HI} . On the other hand, our detection of H I absorption towards PKS 0409–75 demonstrates that using the core-total flux density ratio is also not always representative of the true covering factor (see [Section 5.1](#)).

Although the average spectral noise reached in these observations is similar to that achieved in similar studies using ASKAP-BETA (e.g. [Allison et al. 2015](#); [Moss et al. 2017](#); [Glowacki et al. 2019](#); [Sadler et al. 2020](#)), these studies primarily focused on compact radio sources and therefore assumed a uniform source covering factor, similar to the majority of H I absorption searches carried out with other radio telescopes. Due to the large uncertainties associated with estimating the covering factor when including resolved or highly extended radio sources from the 2-Jy sample, it is challenging to carry out a fair comparison on the detection rate in this sample with previous studies. In the remainder of this paper we focus on the two detections of H I absorption towards PKS 0023–26 and PKS 0409–75.

3.2 H I absorption in PKS 0023–26

PKS 0023–26 is a compact steep spectrum radio source at $z = 0.32188 \pm 0.00004$ ([Santoro et al. 2020](#)) with a linear size of 1.97 kpc ([Tzioumis et al. 2002](#)). The radio source is identified with

Table 2. Fractional absorption ($\Delta S/S_{\text{cont}}$) and H I column density measurements for 2-Jy sources observed with ASKAP-BETA. For sources where no H I absorption was detected we report 3 sigma upper limits per channel and assume a velocity width of 30 km s^{–1} to calculate an upper limit for N_{HI} . Due to the large uncertainties in the covering factor for this sample we present two values of N_{HI} to indicate the range of column densities probed by these observations depending on the assumed C_f . A spin temperature of $T_{\text{spin}} = 500$ K is used throughout.

Source	R	$\frac{\Delta S}{S_{\text{cont}}}$	$N_{\text{HI}} (C_f=R)$ (cm^{-2})	$N_{\text{HI}} (C_f=1)$ (cm^{-2})
PKS 0023–26	1.0	0.0122	1.49×10^{21}	1.49×10^{21}
PKS 0035–02	0.335	<0.050	$< 4.1 \times 10^{21}$	$< 1.37 \times 10^{21}$
PKS 0039–44	-	<0.050	-	$< 1.37 \times 10^{21}$
PKS 0105–16	0.002	<0.014	$< 1.91 \times 10^{23}$	$< 3.83 \times 10^{20}$
PKS 0117–15	-	<0.009	-	$< 2.46 \times 10^{20}$
PKS 0235–19	0.0001	<0.009	$< 2.46 \times 10^{24}$	$< 2.46 \times 10^{20}$
PKS 0252–71	1.0	<0.010	$< 2.73 \times 10^{20}$	$< 2.73 \times 10^{20}$
PKS 0409–75*	-	0.0107	-	2.16×10^{21}
PKS 1136–13	-	<0.0075	-	$< 2.05 \times 10^{20}$
PKS 1151–34	1.0	<0.029	$< 7.93 \times 10^{20}$	$< 7.93 \times 10^{20}$
PKS 1306–09	1.0	<0.0063	$< 1.72 \times 10^{20}$	$< 1.72 \times 10^{20}$
PKS 1547–79	0.002	<0.013	$< 1.78 \times 10^{23}$	$< 3.55 \times 10^{20}$
PKS 1602+01	0.061	<0.0078	$< 3.50 \times 10^{21}$	$< 2.13 \times 10^{20}$
PKS 1938–15	-	<0.012	-	$< 3.28 \times 10^{20}$
PKS 2135–14	0.096	<0.093	$< 2.65 \times 10^{22}$	$< 2.54 \times 10^{21}$
PKS 2135–20	1.0	<0.021	$< 5.74 \times 10^{20}$	$< 5.74 \times 10^{20}$

* A source covering factor of $C_f = 0.3$ was assumed for this source as discussed in [Section 5.1](#).

an $m_v = 19.5$ galaxy ([Wall & Peacock 1985](#)) and deep optical and IR follow-up have found evidence for active star formation ([Tadhunter et al. 2002](#); [Holt et al. 2007](#); [Dicken et al. 2012](#)). Recent

ALMA observations of this source also reveal that it is extremely rich in molecular gas (Morganti et al. 2021).

Observations with ASKAP-BETA reveal H I absorption at 1074.4 MHz. To derive the properties of the H I line we used FLASHfinder³, an automated line finding and characterisation tool, full details of which are described in Allison et al. (2012a). A single Gaussian component with a rest-frame FWHM = $133.5^{+18.9}_{-16.5}$ km s⁻¹, peak optical depth $\tau = 0.0122 \pm 0.0014$ and redshift $z_{\text{HI}} = 0.32184 \pm 0.00003$ provided the best fit to the data. This best fitting model is shown in Fig 2 where the systemic velocity has been set to the optical redshift of $z = 0.32188$ (Santoro et al. 2020). Since PKS 0023–26 is a known CSS source (with Very Long Baseline Interferometry (VLBI) imaging confirming a linear extent < 2 kpc; Tzioumis et al. 2002) we assume a covering factor of 1 and a spin temperature of 500 K to obtain a H I column density of

$$N_{\text{HI}} = 1.49 \times 10^{21} \left(\frac{T_{\text{spin}}}{500\text{K}} \right) \left(\frac{C_{\text{f}}}{1.0} \right)^{-1} \text{cm}^{-2}. \quad (3)$$

H I 21-cm absorption was previously detected in this source by Vermeulen et al. (2003) using the Westerbork Synthesis Radio Telescope (WSRT). Due to the larger sensitivity of the WSRT array compared to ASKAP-BETA, these observations revealed two components of the absorption line: a deeper component centred close to the systemic velocity of the galaxy ($v = -30$ km s⁻¹, $\Delta v = 126$ km s⁻¹ with peak optical depth $\tau = 0.0093$) and a second, shallower component blueshifted from the systemic ($v = -174$ km s⁻¹, $\Delta v = 39$ km s⁻¹ with peak optical depth $\tau = 0.002$)⁴.

Figure 2 overlays these line fits to visually compare with the single Gaussian component identified in the ASKAP-BETA spectrum. The shallower component is not recovered in the ASKAP-BETA observations due to the higher noise levels, but while the velocity width is similar, the deeper component shows a slight change in peak optical depth between the WSRT and ASKAP-BETA observations. This is mostly clearly seen in the residual spectra after subtracting these two different fits as shown in the bottom panel of Figure 2. The uncertainties associated with the peak optical depth measurements indicate they are within 2 sigma and therefore any possible variability is unlikely to be statistically significant. To further verify this, the line parameters reported by Vermeulen et al. (2003) were subtracted from the ASKAP-BETA spectrum and the residual spectrum run through the FLASHfinder line-finding tool to search for evidence of an absorption feature remaining. No significant lines were detected confirming that the measured line parameters are consistent with each other within the noise.

3.3 H I absorption in PKS 0409–75

PKS 0409–75 is a powerful FR II radio galaxy with a projected linear size of 85 kpc (Large et al. 1981; Morganti et al. 1999)⁵. The host galaxy is a magnitude $m_V = 21.6$ galaxy which is resolved into two components and displays extended emission in [OII] $\lambda 3727$ (di Serego Alighieri et al. 1994). Fitting stellar population models to the optical spectrum, Holt et al. (2007) found that PKS 0409–75 has a very young stellar population with an age of approximately 0.02

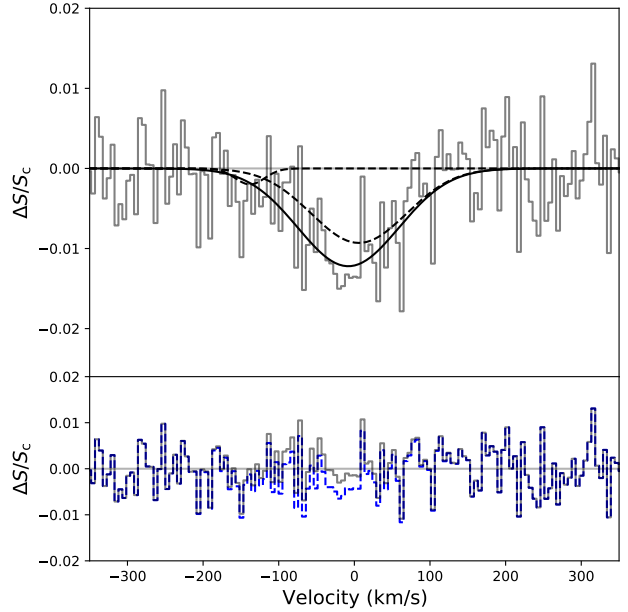


Figure 2. *Top:* H I absorption detected in PKS 0023–26 where the velocity-axis is defined with reference to the optical redshift $z = 0.32188$. The solid line shows the best fitting parameters of a single Gaussian component with FWHM = 133.5 km s⁻¹ and peak optical depth $\tau = 0.0122$. The dashed lines show the line parameters, and the additional component reported by Vermeulen et al. (2003), shifted to the same systemic velocity for comparison. *Bottom:* The residual spectrum after subtraction of the best fitting parameters determined by FLASHfinder (solid grey line) and the residual spectrum after subtraction of the parameters reported in Vermeulen et al. (2003) (blue dashed line).

Gyr. The extended emission in [OII], a young stellar population, and complicated optical structure, point towards recent merger activity in this galaxy.

ASKAP-BETA observations revealed H I absorption detected along the line-of-sight to PKS 0409–75, at a frequency of 848.5 MHz. Using the FLASHfinder line-fitting tool the absorption line is best fit by two Gaussian components as shown in Figure 3; a narrow line with FWHM = $14.8^{+1.1}_{-0.9}$ km s⁻¹, peak redshift $z = 0.67431 \pm 0.00005$ and peak optical depth 0.0050 ± 0.0003 and a broader component with FWHM = $80.1^{+2.2}_{-1.9}$ km s⁻¹, redshift $z = 0.67443 \pm 0.00005$ and peak optical depth 0.0074 ± 0.0001 . However, the most striking feature of this detection is that the H I absorption is at a redshift of $z_{\text{HI}} = 0.674$, offset from the systemic velocity of the host galaxy (determined by the optical redshift of $z = 0.693$) by more than -3300 km s⁻¹.

Such an extreme velocity offset implies that the neutral gas detected via the 21-cm absorption signal is not associated with PKS 0409–75 itself, but more likely originates from a nearby galaxy in the surrounding environment of this powerful radio source. Although there is some evidence for merger-related activity in the host galaxy of PKS 0409–75 (Ramos Almeida et al. 2011), the velocity offset is significantly larger than what is typically associated with tidal features. Tidal features associated with individual galaxies or galaxy pairs are typically less than 200 km s⁻¹ (Bekki et al. 2005; Koribalski 2020) while the spread of tidal debris in galaxy groups

³ https://github.com/drjamesallison/flash_finder

⁴ We note that the rest-frame velocities measured in the WSRT observations are defined from the most accurate redshift available at the time of publication of $z = 0.322$ (di Serego Alighieri et al. 1994)

⁵ PKS 0409–75 is also sometimes referred to as PKS 0410–75 (e.g. in the NASA Extragalactic Database; <https://ned.ipac.caltech.edu/>)

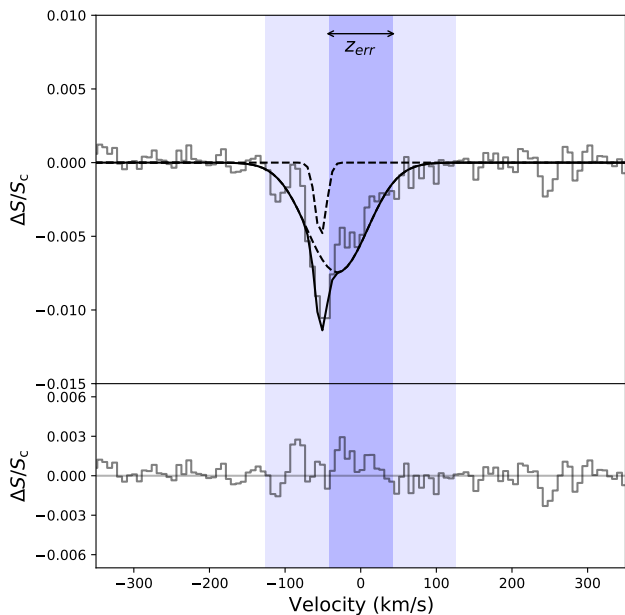


Figure 3. *Top:* Spectrum and best fitting model to the H I absorption line detected towards PKS 0409–75. The dashed lines plot the individual Gaussian components and the solid line shows the combined fit. *Bottom:* Residual spectrum after subtraction of the best fitting parameters shown in the top panel. The velocity axis is given with respect to the optical redshift shown in Section 4.3 with the shaded regions showing the 1- and 3- σ errors ($z_{\text{opt}} = 0.6746 \pm 0.00024$).

or clusters can be larger, up to $\sim 500 \text{ km s}^{-1}$ and $\sim 1000 \text{ km s}^{-1}$ respectively (Saponara et al. 2018; Lee-Waddell et al. 2019; Namumba et al. 2021). A velocity difference of more than 3000 km s^{-1} has not been observed and is unlikely in a bound system.

Previous deep optical imaging of PKS 0409–75 presented in Ramos Almeida et al. (2011) shows evidence for a separate galaxy co-incident with the southern radio lobe, however, no spectroscopic information was available to indicate if this galaxy is at the same redshift as the H I absorption line.

4 OPTICAL FOLLOW-UP OF PKS 0409–75

To verify that this galaxy observed in previous optical images could be a possible association of the H I feature, additional imaging and longslit spectroscopy were obtained using the Gemini-South telescope.

4.1 Optical Imaging

Follow-up multi-band imaging of PKS 0409–75 was carried out on 2017 August 28 using the Gemini Multi-Object Spectrograph (GMOS) on the Gemini-South 8m telescope (ProgID number GS-2017B-Q-63). The 5.5 arcmin field was centred on PKS 0409–75 and a 300 second exposure time used in each of the g' , r' and i' filters with the aim of reaching limiting magnitudes of approximately $g'=23.9$, $r'=23.5$ and $i'=23.3$. The total exposure time in each band was split into 4×75 second individual exposures to aid in cosmic

ray rejection. The seeing conditions during the observations ranged from 0.7 – 0.8 arcsec.

The data were reduced using the standard Gemini IRAF packages and a gri-colour image made using the ASTROPY and APLPY packages (The Astropy Collaboration et al. 2018; Robitaille 2019). No standard stars were observed during the imaging observations, so the median photometric zero-points measured for each GMOS-S filter⁶ were used when calculating optical magnitudes.

4.2 Longslit Spectroscopy

Longslit observations of PKS 0409–75 were taken with the Gemini Multi-Object Spectrograph (GMOS) on the Gemini-South telescope on 2017 September 16 as part of the same observing programme (GS-2017B-Q-63). In order to distinguish between the two possible optical associations detected in previous Gemini imaging we orientated a 1.5 arcsec slit at a position angle of 133 deg to obtain spectra of both the host galaxy of PKS 0409–75 and the nearby galaxy at the position of the eastern radio lobe.

The observations were taken using the R400 grating with central wavelengths of 700 and 705 nm which allowed for dithering across the CCD chip gaps to obtain continuous spectral coverage from 490–910 nm. Using 2x2 binning resulted in pixel sizes of 0.16 arcsec spatially and 0.15 nm in the spectral direction. 6×900 s exposures were taken for each central wavelength leading to a total on source integration time of 3 hr. GCALflat observations were taken in between the science observations while bias images and CuAr arc exposures were taken at the end of the night.

Standard Gemini IRAF tasks were used for bias subtraction, flat-fielding, wavelength calibration and sky subtraction for each exposure independently. The 2D spectra for each configuration were then combined to increase the S/N before extracting two apertures for each combined 2D spectrum; one at the position of the host galaxy of PKS 0409–75 (denoted ‘galaxy A’ hereafter) and another at the position of the galaxy at the position of the eastern radio lobe (‘galaxy B’). The data were flux calibrated using an observation of a standard star (CD-34 241) taken on 2017 August 21. No telluric calibration was performed meaning the atmospheric A-band is still evident in the resulting spectra. Once calibrated, the 1D spectra were combined using the IRAF SCOMBINE task.

The reduced spectra of both galaxies were then run through the MARZ web-based redshifting software (Hinton et al. 2016) to identify the redshift of both sources.

4.3 Optical properties of PKS 0409–75

A 3-colour image compiled from g' , r' and i' band observations is shown in Figure 4 overlaid with contours from 8 GHz Australia Telescope Compact Array (ATCA) observations (Morganti et al. 1999), which shows an elliptical galaxy at the position of the southern radio lobe. For ease of reference we denote the host galaxy of PKS 0409–75 ‘galaxy A’ and the galaxy coincident with the southern radio lobe ‘galaxy B’ hereafter. We also note that the radio contours shown in Figure 4 have much higher spatial resolution due to the higher observed frequency and longer baselines provided by the ATCA, resulting in a synthesised beam of $0''.7 \times 1''.2$ compared to the $\sim 1''.5$ resolution provided by ASKAP-BETA. The continuum source is unresolved in the ASKAP-BETA observations presented here and therefore we cannot directly determine if the absorption

⁶ <https://www.gemini.edu/instrumentation/gmos/calibrations#PhotStand>

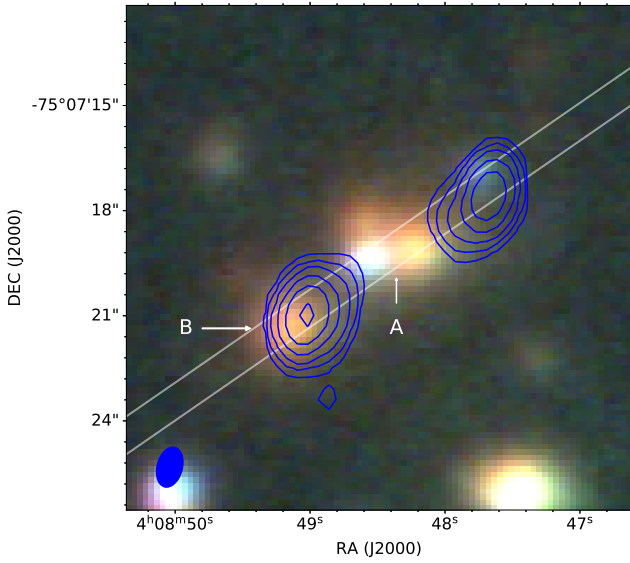


Figure 4. Gemini GMOS *gri*-image of PKS 0409–75 and surrounding galaxies. The double nucleus in PKS 0409–75 reported in Ramos Almeida et al. (2011) is clearly visible (galaxy A), as is a possible companion galaxy to the south-east (galaxy B). Radio contours from higher resolution 8 GHz ATCA observations are overlaid in blue, with the synthesised beam shown in the bottom left corner. The grey lines mark the position of the slit used in the Gemini-GMOS longslit observations discussed in Section 4.3. Standard image orientation is used with North up and East to the left.

line is detected along the line of sight to one of the radio lobes from the ASKAP-BETA data alone.

Figure 5 shows the spectra obtained from the Gemini-GMOS observations of galaxies A (top) and B (bottom). Both the optical imaging and spectroscopy confirm the complex nature of the host galaxy of PKS 0409–75 (galaxy A), with the 3-colour (*gri*) image showing clear evidence for a double nucleus as previously shown in Ramos Almeida et al. (2011). The spectrum of galaxy A is similar to that observed by di Serego Alighieri et al. (1994) and also shows extended [OII] and [OIII] emission as discussed in Holt et al. (2007).

The redder optical colours for galaxy B on the other hand suggest that this is more likely to be a early-type galaxy. The spectrum of galaxy B shows [OII] emission, as well as evidence for weak [OIII] emission and the CaII H and K absorption lines, placing the source at a redshift $z = 0.6746 \pm 0.00024$. This is very similar to the redshift of the absorption line detected with ASKAP-BETA (within $\sim 50 \text{ km s}^{-1}$), confirming galaxy B as the association of the H I 21-cm absorption line.

5 DISCUSSION

5.1 Properties of the H I absorbing galaxy towards PKS 0409–75

Our targeted follow-up observations of this source at optical-wavelengths indicate that the H I 21-cm absorption system detected with ASKAP-BETA is associated with galaxy B in front of the eastern radio lobe of PKS 0409–75. Using the redshift of galaxy B ($z = 0.6746 \pm 0.00024$) as the systemic velocity, Figure 3 shows that the H I feature detected is slightly blueshifted compared to the systemic velocity, but consistent within the redshift error of 42 km s^{-1}

derived from the optical follow-up⁷. The fact that most of the 21-cm absorption is observed blueward of the systemic velocity could indicate that only a portion of the H I in galaxy B is being detected in absorption. This is somewhat verified by the optical image shown in Figure 4 which shows that galaxy B is not entirely in front of the background radio lobe of PKS 0409–75, but higher resolution images in both the radio and optical are needed to confirm this. The peak of the radio emission is offset from the centroid of galaxy B meaning that an offset of $\sim 75 \text{ km s}^{-1}$ might be expected for a typical galaxy rotation velocity of $\sim 150 \text{ km s}^{-1}$ if this sight-line was probing only a small fraction of the galaxy (Reeves et al. 2016). The width of the H I line is broader than typically observed for intervening galaxies where the mean of the distribution is $\sim 30 \text{ km s}^{-1}$ (Curran et al. 2016), however this could be explained by the fact that diffuse continuum emission from the background radio lobe could be illuminating multiple sight-lines through galaxy B. We also looked for evidence of rotation along the slit, but as a larger aperture was needed to get sufficient S/N to detect the weak emission lines there was no clear indication of any rotation.

To calculate the H I column density we assume a covering factor of 0.3, roughly estimated based on the flux ratio between the two radio lobes (the eastern lobe contains $\sim 60\%$ of the total flux), combined with the fact that galaxy B intercepts approximately half of the radio lobe as shown in Figure 4. Again assuming a spin temperature $T_{\text{spin}} = 500 \text{ K}$ and using the measured integrated optical depth of 0.71 ± 0.01 , Equations 1 and 2 give a 21-cm H I column density of

$$N_{\text{HI}} = 2.16 \times 10^{21} \left(\frac{T_{\text{spin}}}{500\text{K}} \right) \left(\frac{C_{\text{f}}}{0.3} \right)^{-1} \text{ cm}^{-2}. \quad (4)$$

We estimate a star-formation rate of $1.24 M_{\odot} \text{ yr}^{-1}$ using the Penalized Pixel-Fitting (pPXF) software (Cappellari 2017) to fit and measure the flux of the [OII] emission and following the Kennicutt relation (Kennicutt 1998). Since the balmer lines were not detected in the longslit observations it was not possible to do any extinction correction when calculating the SFR so this value represents a rough estimate. It should also be noted that [OII] emission is not typically the best tracer to estimate the star-formation rate due to contamination of AGN or shocks which can also produce [OII] emission (Maddox 2018). However, there is no strong evidence for AGN activity in galaxy B and the moderate amount of star-formation is consistent both with the H I column density and typical SFR of early-type galaxies (Serra et al. 2012; Davis et al. 2014).

Using the SExtractor source finding software (Bertin & Arnouts 1996), we measure optical magnitudes of $g' = 21.32 \pm 0.11$, $r' = 20.13 \pm 0.04$ and $i' = 18.90 \pm 0.03$ using the AUTOMAG option for the absorbing galaxy (galaxy B). The r' -band image was used as the detection image for all filters to ensure that a common aperture was used for the source finding. These optical magnitudes were corrected for Galactic extinction using A_{λ} values given by Schlafly & Finkbeiner (2011) and K-corrected to give a restframe ($g' - r'$) colour of 1.12 mag using the method in Chilingarian et al. (2010). Galaxy B was also detected in the VISTA Hemisphere Survey (VHS; McMahon et al. 2013, 2021) with source name VHS J040849.12–750721.5 and magnitudes $J = 17.10$ and $K_s = 15.48$ mag. Using ($g' - r'$) colour combined with the J -/ K_s -band magnitudes, and following the stellar M/L ratios as a function of optical–NIR colours (Bell et al. 2003) we estimate the stellar mass

⁷ The redshift error is estimated using the Penalized Pixel-Fitting (pPXF) software (Cappellari 2017)

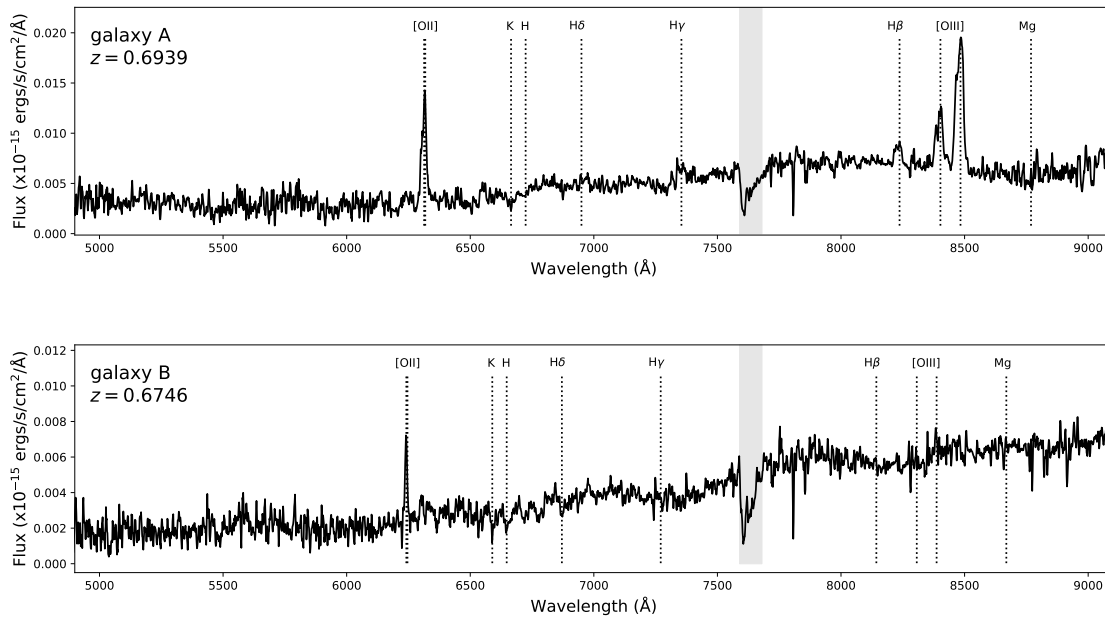


Figure 5. Gemini-South GMOS longslit spectra of PKS 0409–75. The top panel shows the spectrum for the host galaxy (galaxy A in Fig 4) and the bottom panel shows the spectrum of galaxy B. Both spectra are shown in the observed frame with the dashed lines marking commonly observed lines at the redshift of each source ($z = 0.6939$ and $z = 0.6746$ for sources A and B respectively) and show where these features would lie at the observed redshift. Not all of these features are necessarily evident in the spectrum. The grey shaded area corresponds to the A-band atmospheric absorption feature.

of galaxy B to be approximately $3.2 - 6.8 \times 10^{11} M_{\odot}$. At this stellar mass, the optical colours are slightly redder (~ 0.1 dex) than that of typical red sequence galaxies in low-density environments (Hogg et al. 2004). Both the SFR and stellar mass estimates assume a modified Salpeter initial mass function (Kennicutt 1983; Bell & de Jong 2001).

In summary, the H I absorption line detected with ASKAP is associated with an early-type galaxy along the line-of-sight to the radio lobe of PKS 0409–75. The H I column density is similar to column densities observed in some nearby early-type galaxies, and consistent with H I emission line studies that show $\sim 40\%$ of early-type galaxies show H I emission (Serra et al. 2012). The optical colours and stellar mass are also similar to that observed in samples of Luminous Red Galaxies (LRGs) at $z \sim 0.7$ (Maraston et al. 2013; Ching et al. 2017).

5.2 Polarisation properties of PKS 0409–75

Previous narrow-band radio polarization observations of PKS 0409–75 at 3cm and 6cm showed an asymmetry in the fractional polarization and Faraday rotation between the two radio lobes (Morganti et al. 1999). More specifically, the observed Faraday rotation, Rotation Measure (RM; the integral of the line-of-sight magnetic field weighted by thermal electron density) of the eastern lobe exceeds that of the western lobe by approximately 300 rad/m^2 . While this difference could be produced within or in the vicinity of the lobes, the presence of coherent magnetic fields in the intervening galaxy towards the eastern lobe could also be responsible for the observed Faraday rotation difference. The presence of small-scale turbulent magnetic fields in the intervening galaxy could probably explain the stronger depolarization seen towards the eastern lobe.

Assuming that the RM difference between the lobes can be fully attributed to the absorber galaxy, and using an ionization fraction of 0.1 (He et al. 2013) to convert neutral column density to electron column density, the coherent magnetic field strength, B , in the absorber galaxy can be estimated as

$$\frac{B}{14.5 \mu\text{G}} = \left(\frac{\Delta\text{RM}_{\text{rest-frame}}}{804.3 \text{ rad m}^{-2}} \right) \left(\frac{T_{\text{spin}}}{500\text{K}} \right)^{-1}. \quad (5)$$

A spin temperature T_{spin} of 500 K, rest-frame Faraday rotation difference between the two lobes $\Delta\text{RM}_{\text{rest-frame}}$ of 804.3 rad m^{-2} corresponds to a coherent magnetic field strength of $14.5 \mu\text{G}$ in the absorber galaxy. The derived magnetic field strength in the $z = 0.674$ absorber galaxy is broadly consistent with the total magnetic field strengths measured in local spiral galaxies (Beck & Wielebinski 2013; Beck 2015), as well as the large-scale coherent disk magnetic field strength measured in a $z = 0.439$ galaxy (Mao et al. 2017). However, this estimated field strength is higher than that expected in elliptical galaxies (Seta et al. 2021). A more in-depth study of the broadband polarimetric properties of PKS 0409–75, including a more detailed estimation of the magnetic fields in the absorber galaxy and its implications on the build-up of galactic magnetic fields over cosmic time will be presented in Seta et al. (in preparation).

5.3 The detection of H I absorption against a radio lobe

Only a handful of H I absorption lines have been detected against the lobes of radio galaxies, primarily due to selection effects of previous samples that have focused on compact radio sources where the chances of detecting H I absorption within the host galaxy of the radio source are much greater. The few detections of H I absorption

against a radio lobe have been discovered serendipitously, similar to the case presented here, rather than from a comprehensive survey searching for absorption against extended radio sources.

A recent study by [Murthy et al. \(2020\)](#) reported H I absorption against the radio lobe of 3C 433. In that case, the absorber is a faint disc galaxy with stellar mass of $\sim 10^{10} M_{\odot}$ blueshifted by only $\sim 50 \text{ km s}^{-1}$ from the systemic velocity of the host galaxy, but has a similar line width of $\sim 80 \text{ km s}^{-1}$. Based on this small difference in velocity, combined with some evidence of disturbed morphology in the southern radio lobe led the authors to suggest that the radio lobe could be interacting with the absorbing galaxy. Similar detections of H I absorption against extended radio sources have been detected in nearby galaxies 3C234 ([Pihlström 2001](#)) and B2 1321+31 ([Emonts 2006](#)), again where the measured velocity of the H I absorption signature is very close to the systemic velocity of the radio AGN host galaxy.

The most distant H I absorption line against a radio lobe detected prior to this discovery was in the radio galaxy PKS 1649–062 at $z = 0.236$ ([Curran et al. 2011](#)). In this case the H I absorption is redshifted 116 km s^{-1} compared to the systemic velocity, with the authors suggesting that the absorber is an intervening galaxy gravitationally bound to the system or possibly associated that a large galactic disc with $r \approx 200 \text{ kpc}$ in PKS 1649–062 ([Curran et al. 2011](#)). These examples all highlight that the detection of 21-cm absorption lines in radio galaxies can trace a number of different situations, and additional multi-wavelength data, especially in the optical, is often vital in the analysis and interpretation of these systems.

Unlike these previous detections, in PKS 0409–75 the velocity offset of $\sim 3300 \text{ km s}^{-1}$ is too large for the radio lobe to be directly impacting the absorbing galaxy. Instead, the 21-cm absorption line detected towards this powerful radio galaxy is associated with a foreground galaxy in front of the south-eastern radio lobe.

5.4 Implications for large absorption line surveys

Despite being one of the brightest sources in the radio sky, this is the first time H I absorption has been searched for in this radio source. One reason for this is the fact that as a clearly extended radio source without a strong radio core, PKS 0409–75 would generally not have been included in typical searches for H I absorption, but a more significant reason is our ability to now search for the 21-cm H I line in absorption over a wide bandwidth at all redshifts between $0.4 < z < 1.0$ with the advent of the Australian Square Kilometre Array Pathfinder (ASKAP). This allows us to probe the neutral gas properties of galaxies at these intermediate redshifts for the first time (see e.g. [Allison et al. 2015](#); [Sadler et al. 2020](#); [Allison 2021](#)), bridging the gap between H I studies at lower redshifts (e.g. [Darling et al. 2011](#)), and QSO Damped Lyman Alpha studies at higher redshifts ([Kanevar et al. 2014](#); [Neeleman et al. 2016](#); [Rao et al. 2017](#)).

The detection of H I absorption against the lobe of PKS 0409–75 gives some insight into the range of H I absorption lines that could be detected by upcoming large H I 21-cm absorption line surveys being carried out with SKA pathfinders such as the First Large Absorption Line Survey in H I (FLASH; [Allison et al. 2021](#)) and the MeerKAT Absorption Line Survey (MALS; [Gupta et al. 2016](#)) which will explore intermediate redshifts from $0.4 < z < 1.5$ in addition to surveys such as the Search for H I Absorption with AperTIF (SHARP; e.g. [Adams & van Leeuwen 2019](#)) and the Wide-field ASKAP L-band Legacy All-sky Blind survey (WALLABY; [Koribalski et al. 2020](#)) which will detect H I 21-cm absorption at

redshifts $0 < z < 0.26$. While the sample size presented here is too small to extrapolate the expected detection rate of H I towards extended radio sources, we note that PKS 0409–75 is one of five objects in the sample that have clearly extended radio structure with no detectable radio emission from the core. Searching for absorption towards all bright radio sources regardless of underlying source structure over a wide area of sky, such as planned for the upcoming FLASH survey, will provide the first estimate of the typical detection rate towards extended radio sources. This study also highlights the need for deep multi-wavelength follow-up observations to understand the properties of H I absorbers that will be detected in these large surveys.

6 CONCLUSIONS

We have carried out a search for 21-cm H I absorption against 16 bright southern radio sources with $0.2 < z < 0.7$ using ASKAP-BETA, the commissioning array of the Australian Square Kilometre Array Pathfinder. This study revealed two detections of H I absorption; one in the compact steep spectrum source PKS 0023–26 at $z = 0.322$ and another towards the radio galaxy PKS 0409–75. The former shows similar line properties to that reported by [Vermeulen et al. \(2003\)](#), with no significant evidence for variability in the H I line. The absorption towards PKS 0409–75 at $z = 0.674$ has not been detected previously and is blueshifted from the systemic velocity of the host galaxy by $\sim 3300 \text{ km s}^{-1}$. Follow-up optical imaging and spectroscopy with GMOS on Gemini-South confirmed that the H I absorption is associated with a foreground galaxy in front of the eastern radio lobe. Using the optical and radio data combined we estimate this galaxy to have a stellar mass of $3.2\text{--}6.8 \times 10^{11} M_{\odot}$ and an H I column density of $2.16 \times 10^{21} \text{ cm}^{-2}$. Using archival polarisation measurements of PKS 0409–75 from [Morganti et al. \(1999\)](#), we provide an estimate of the magnetic field in the foreground galaxy of $\sim 14.5 \mu\text{G}$, giving the first estimate of the magnetic field of a normal galaxy at $z \sim 0.7$.

Although only a small sample was searched for H I absorption in this work, it provides a pilot study of what could be detected by future large absorption line surveys such as the First Large Absorption Line Survey in H I ([Allison et al. 2021](#)), currently being carried out with ASKAP. Having a sufficiently bright background radio source was the primary selection criteria used to define this sample, with no further constraints on the source size or optical properties (with the exception that the H I absorption line would be in the frequency range observable with ASKAP). The result of this broader selection criteria led to the detection of absorption towards the lobe of PKS 0409–75 as its extended radio structure and large velocity offset from the host galaxy means that it would likely have been excluded from many previous searches for H I absorption.

ACKNOWLEDGEMENTS

We thank Jesse van der Sande for useful discussions on the optical data analysis presented here and the anonymous referee for helpful suggestions that improved the quality of the paper. Optical observations for this paper were carried out under the Gemini programme GS-2017B-Q-63 and we thank the telescope operators and staff for carrying out these observations. We also thank CSIRO operations and engineering staff who assisted in obtaining the ASKAP-BETA observations. Parts of this research were conducted by the Australian

Research Council Centre of Excellence for All-sky Astrophysics in 3D (ASTRO 3D) through project number CE170100013.

The Australian SKA Pathfinder is part of the Australia Telescope National Facility which is managed by CSIRO. Operation of ASKAP is funded by the Australian Government with support from the National Collaborative Research Infrastructure Strategy. ASKAP uses the resources of the Pawsey Supercomputing Centre. Establishment of ASKAP, the Murchison Radio-astronomy Observatory and the Pawsey Supercomputing Centre are initiatives of the Australian Government, with support from the Government of Western Australia and the Science and Industry Endowment Fund. We acknowledge the Wajarri Yamatji people as the traditional owners of the Observatory site.

This research made use of APLpy, an open-source plotting package for Python (Robitaille & Bressert 2012; Robitaille 2019) and Astropy,⁸ a community-developed core Python package for Astronomy (Astropy Collaboration et al. 2013; The Astropy Collaboration et al. 2018).

DATA AVAILABILITY

All data underlying this article will be shared on reasonable request to the corresponding author. The optical data are publicly available for download through the Gemini archive under project code GS-2017B-Q-63 at <https://archive.gemini.edu/searchform>.

REFERENCES

- Adams E. A. K., van Leeuwen J., 2019, *Nature Astronomy*, **3**, 188
- Aditya J. N., 2019, *MNRAS*, **482**, 5597
- Aditya J. N. H. S., Kanekar N., Kurapati S., 2016, *MNRAS*, **4012**, 4000
- Aditya J. N. H. S., Jorgenson R., Joshi V., Singh V., An T., Chandola Y., 2021, *MNRAS*, **500**, 998
- Allison J. R., 2021, *MNRAS*, **503**, 985
- Allison J. R., Sadler E. M., Whiting M. T., 2012a, *PASA*, **29**, 221
- Allison J. R., et al., 2012b, *MNRAS*, **423**, 2601
- Allison J. R., et al., 2015, *MNRAS*, **1267**, 1249
- Allison J. R., et al., 2020, *MNRAS*, **494**, 3627
- Allison J. R., et al., 2021, arXiv e-prints, p. [arXiv:2110.00469](https://arxiv.org/abs/2110.00469)
- Astropy Collaboration et al., 2013, *A&A*, **558**, A33
- Bahcall J. N., Ekers R. D., 1969, *ApJ*, **157**, 1055
- Beck R., 2015, *A&ARv*, **24**, 4
- Beck R., Wiebeleski R., 2013, *Magnetic Fields in Galaxies*. Springer Netherlands, Dordrecht, p. 641, doi:[10.1007/978-94-007-5612-0_13](https://doi.org/10.1007/978-94-007-5612-0_13)
- Bekki K., Koribalski B. S., Kilborn V. A., 2005, *MNRAS*, **363**, L21
- Bell E. F., de Jong R. S., 2001, *ApJ*, **550**, 212
- Bell E. F., McIntosh D. H., Katz N., Weinberg M. D., 2003, *ApJS*, **149**, 289
- Bertin E., Arnouts S., 1996, *A&AS*, **117**, 393
- Beswick R. J., Pedlar A., Holloway A. J., 2002, *MNRAS*, **329**, 620
- Beswick R. J., Peck A. B., Taylor G. B., Giovannini G., 2004, *MNRAS*, **352**, 49
- Cappellari M., 2017, *MNRAS*, **466**, 798
- Chandola Y., Gupta N., Saikia D. J., 2013, *MNRAS*, **429**, 2380
- Chandola Y., Saikia D. J., Li D., 2020, *MNRAS*, **494**, 5161
- Chilingarian I. V., Melchior A.-L., Zolotukhin I. Y., 2010, *MNRAS*, **405**, 1409
- Ching J. H. Y., et al., 2017, *MNRAS*, **464**, 1306
- Chowdhury A., Kanekar N., Chengalur J. N., 2020, *ApJ*, **900**, L30
- Condon J. J., 1989, *ApJ*, **338**, 13
- Condon J. J., Cotton W. D., Greisen E. W., Yin Q. F., Perley R. A., Taylor G. B., Broderick J. J., 1998, *AJ*, **115**, 1693
- Condon J. J., Matthews A. M., Broderick J. J., 2019, *ApJ*, **872**, 148
- Curran S. J., Whiting M. T., Wiklind T., Webb J. K., Murphy M. T., Purcell C. R., 2008, *MNRAS*, **391**, 765
- Curran S. J., Whiting M. T., Webb J. K., Athreya R., 2011, *MNRAS*, **414**, L26
- Curran S. J., Whiting M. T., Tanna A., Sadler E. M., Pracy M. B., Athreya R., 2012, *MNRAS*, **9**, 1
- Curran S. J., Duchesne S. W., Divoli A., Allison J. R., 2016, *MNRAS*, **462**, 4197
- Darling J., Macdonald E. P., Haynes M. P., Giovanelli R., 2011, *ApJ*, **742**, 60
- Dasyra K. M., Combes F., 2012, *A&A*, **541**, L7
- Davis T. A., et al., 2014, *MNRAS*, **444**, 3427
- Dicken D., Tadhunter C., Morganti R., Buchanan C., Oosterloo T., Axon D., 2008, *ApJ*, **678**, 712
- Dicken D., et al., 2012, *ApJ*, **745**, 172
- Dickey J. M., Strasser S., Gaensler B. M., Haverkorn M., Kavars D., McClure-Griffiths N. M., Stil J., Taylor A. R., 2009, *ApJ*, **693**, 1250
- Dutta R., Srianand R., Gupta N., 2018, *MNRAS*, **480**, 947
- Dutta R., Srianand R., Gupta N., 2019, *MNRAS*, **489**, 1099
- Dutta R., Raghunathan S., Gupta N., Joshi R., 2020, *MNRAS*, **491**, 838
- Emonts B. H. C., 2006, PhD thesis, University of Groningen
- Geréb K., Maccagni F. M., Morganti R., Oosterloo T. A., 2015, *A&A*, **575**, 44
- Glowacki M., et al., 2017, *MNRAS*, **467**, 2766
- Glowacki M., et al., 2019, *MNRAS*, **489**, 4926
- Gupta N., Saikia D. J., 2006, *MNRAS*, **742**, 738
- Gupta N., et al., 2016, in *MeerKAT Science: On the Pathway to the SKA*. p. 14 ([arXiv:1708.07371](https://arxiv.org/abs/1708.07371))
- Gupta Y., et al., 2017, *Current Science*, **113**, 707
- Hale C. L., et al., 2021, arXiv e-prints, p. [arXiv:2109.00956](https://arxiv.org/abs/2109.00956)
- He C., Ng C. Y., Kaspi V. M., 2013, *ApJ*, **768**, 64
- Herrera-Camus R., et al., 2020, *A&A*, **635**, A47
- Hinton S. R., Davis T. M., Lidman C., Glazebrook K., Lewis G. F., 2016, *Astronomy and Computing*, **15**, 61
- Hogg D. W., et al., 2004, *ApJ*, **601**, L29
- Holt J., Tadhunter C., Morganti R., Bellamy M., González Delgado R. M., Tzioumis A., Inskip K. J., 2006, *MNRAS*, **370**, 1633
- Holt J., Tadhunter C. N., González Delgado R. M., Inskip K. J., Rodriguez Zaurin J., Emonts B. H. C., Morganti R., Wills K. A., 2007, *MNRAS*, **381**, 611
- Hotan A. W., et al., 2014, *PASA*, **31**, e041
- Hotan A. W., et al., 2021, *PASA*, **38**, 1
- Jonas J., MeerKAT Team 2016, in *MeerKAT Science: On the Pathway to the SKA*. p. 1
- Kanekar N., Prochaska J. X., Ellison S. L., Chengalur J. N., 2009a, *MNRAS*, **396**, 385
- Kanekar N., Smette A., Briggs F. H., Chengalur J. N., 2009b, *ApJ*, **705**, L40
- Kanekar N., et al., 2014, *MNRAS*, **438**, 2131
- Kennicutt R. C. J., 1983, *ApJ*, **272**, 54
- Kennicutt Robert C. J., 1998, *ApJ*, **498**, 541
- Koribalski B. S., 2020, arXiv e-prints, p. [arXiv:2002.07312](https://arxiv.org/abs/2002.07312)
- Koribalski B. S., et al., 2020, *Ap&SS*, **365**, 118
- Large M. I., Mills B. Y., Little A. G., Crawford D. F., Sutton J. M., 1981, *MNRAS*, **194**, 693
- Lee-Waddell K., et al., 2019, *MNRAS*, **487**, 5248
- Maccagni F. M., Morganti R., Oosterloo T. A., Mahony E. K., 2014, *A&A*, **67**, 4
- Maccagni F. M., Morganti R., Oosterloo T. A., Geréb K., Maddox N., 2017, *A&A*, p. 1
- Maddox N., 2018, *MNRAS*, **480**, 5203
- Mao S. A., et al., 2017, *Nature Astronomy*, **1**, 621
- Maraston C., et al., 2013, *MNRAS*, **435**, 2764
- Mauch T., Sadler E. M., 2007, *MNRAS*, **375**, 931
- McConnell D., et al., 2016, *PASA*, **33**
- McConnell D., et al., 2020, *PASA*, **37**, 1
- McMahon R. G., Banerji M., Gonzalez E., Kopsosov S. E., Bejar V. J., Lodieu N., Rebolo R., VHS Collaboration 2013, *The Messenger*, **154**, 35

⁸ <http://www.astropy.org>

- McMahon R. G., Banerji M., Gonzalez E., Kuposov S. E., Bejar V. J., Lodieu N., Rebolo R., VHS Collaboration 2021, *VizieR Online Data Catalog*, p. II/367
- Mingo B., Hardcastle M. J., Croston J. H., Dicken D., Evans D. A., Morganti R., Tadhunter C., 2014, *MNRAS*, 440, 269
- Morganti R., Oosterloo T., 2018, *A&ARv*, 26, 1
- Morganti R., Killeen N., Tadhunter C., 1993, *MNRAS*, 263, 1023
- Morganti R., Killeen N., Tadhunter C., Aiudi R., Jones P., Villar-Martin M., 1999, *MNRAS*, 140, 355
- Morganti R., Oosterloo T. A., Tadhunter C. N., van Moorsel G., Killeen N., Wills K. A., 2001, *MNRAS*, 323, 331
- Morganti R., Tadhunter C., Oosterloo T. A., 2005, *A&A*, 13, 9
- Morganti R., Fogasy J., Paragi Z., Oosterloo T., Orienti M., 2013, *Science*, 341, 1082
- Morganti R., Sadler E. M., Curran S., 2015, in *Advancing Astrophysics with the Square Kilometre Array (AASKA14)*, p. 134 ([arXiv:1501.01091](https://arxiv.org/abs/1501.01091))
- Morganti R., Oosterloo T., Tadhunter C., Bernhard E. P., Oonk J. B. R., 2021, arXiv e-prints, p. [arXiv:2109.13516](https://arxiv.org/abs/2109.13516)
- Moss V. A., et al., 2017, *MNRAS*, 471, 2952
- Murray C. E., Stanimirović S., Goss W. M., Heiles C., Dickey J. M., Babler B., Kim C.-G., 2018, *ApJS*, 238, 14
- Murthy S., Morganti R., Emonts B., Villar-Martín M., Oosterloo T., Peletier R., 2020, *A&A*, 643, A74
- Murthy S., Morganti R., Oosterloo T., Maccagni F. M., 2021, arXiv e-prints, p. [arXiv:2108.08122](https://arxiv.org/abs/2108.08122)
- Namumba B., et al., 2021, *MNRAS*, 505, 3795
- Neeleman M., Prochaska J. X., Ribaldo J., Lehner N., Howk J. C., Rafelski M., Kanekar N., 2016, *ApJ*, 818, 113
- Oosterloo T., Verheijen M. A. W., van Cappellen W., Bakker L., Heald G., Ivashina M., 2009, in *Wide Field Astronomy & Technology for the Square Kilometre Array*, p. 70 ([arXiv:0912.0093](https://arxiv.org/abs/0912.0093))
- Oosterloo T., Morganti R., Tadhunter C., Raymond Oonk J. B., Bignall H. E., Tzioumis T., Reynolds C., 2019, *A&A*, 632, A66
- Perley R. A., Chandler C. J., Butler B. J., Wrobel J. M., 2011, *ApJ*, 739, L1
- Pihlström Y., 2001, PhD thesis, Chalmers University of Technology
- Pihlstrom Y. M., Conway J. E., Vermeulen R. C., 2003, *A&A*, 881, 871
- Ramos Almeida C., Tadhunter C. N., Inskip K. J., Morganti R., Holt J., Dicken D., 2011, *MNRAS*, 410, 1550
- Rao S. M., Turnshek D. A., Sardane G. M., Monier E. M., 2017, *MNRAS*, 471, 3428
- Reeves S. N., et al., 2016, *MNRAS*, 457, 2613
- Robitaille T., 2019, APLpy v2.0: The Astronomical Plotting Library in Python, [doi:10.5281/zenodo.2567476](https://doi.org/10.5281/zenodo.2567476)
- Robitaille T., Bressert E., 2012, APLpy: Astronomical Plotting Library in Python (ascl:1208.017)
- Sadler E. M., et al., 2020, *MNRAS*, 499, 4293
- Santoro F., Tadhunter C., Baron D., Morganti R., Holt J., 2020, *A&A*, 644, A54
- Saponara J., Koribalski B. S., Benaglia P., Fernández López M., 2018, *MNRAS*, 473, 3358
- Schlafly E. F., Finkbeiner D. P., 2011, *ApJ*, 737, 103
- Schulz R., Morganti R., Nyland K., Paragi Z., Mahony E. K., Oosterloo T., 2018, *A&A*, 617, 1
- Schulz R., Morganti R., Nyland K., Paragi Z., Mahony E. K., Oosterloo T., 2021, *A&A*, 647, A63
- Serra P., et al., 2012, *MNRAS*, 422, 1835
- Seta A., Rodrigues L. F. S., Federrath C., Hales C. A., 2021, *ApJ*, 907, 2
- Tadhunter C. N., Morganti R., di Serego-Alighieri S., Fosbury R. A. E., Danziger I. J., 1993, *MNRAS*, 263, 999
- Tadhunter C., Dickson R., Morganti R., Robinson T. G., Wills K., Villar-Martin M., Hughes M., 2002, *MNRAS*, 330, 977
- Tadhunter C., Morganti R., Rose M., Oonk J. B. R., Oosterloo T., 2014, *Nature*, 511, 440
- The Astropy Collaboration et al., 2018, *AJ*, 156, 123
- Tremblay G. R., et al., 2016, *Nature*, 534, 218
- Tzioumis A., et al., 2002, *A&A*, 392, 841
- Vermeulen R. C., et al., 2003, *A&A*, 404, 861
- Wall J. V., Peacock J. A., 1985, *MNRAS*, 216, 173
- Wilson W. E., et al., 2011, *MNRAS*, 416, 832
- di Serego Alighieri S., Danziger I., Morganti R., Tadhunter C. N., 1994, *MNRAS*, 269, 998
- van Gorkom J. H., Knapp G., Ekers R., Ekers D. D., Laing R. A., Polk K. S., 1989, *AJ*, 97, 708

APPENDIX A: ASKAP-BETA OBSERVATIONS

ASKAP-BETA observations of 16 sources selected from the 2-Jy sample of southern radio galaxies were observed between November 2014 and February 2016. Table A1 details the observation data, schedule block ID number (SBID) and median spectral noise across the full bandwidth for each observation of this sample.

APPENDIX B: ASKAP-BETA SPECTRA

ASKAP-BETA provided a full bandwidth of 304 MHz covering a redshift range of $0.4 < z < 1$ for objects observed at a central frequency of 863.5 MHz. Figure B1 shows an example spectrum obtained from one observation of PKS 0409-75 demonstrating the full bandwidth covered for all observations and the lack of radio frequency interference at these frequencies. The top axis shows the redshift of the 21-cm H I line and the bottom axis shows the frequency shifted into the barycentric reference frame (ν_{bary}).

This paper has been typeset from a $\text{\TeX}/\text{\LaTeX}$ file prepared by the author.

Table A1. ASKAP-BETA observations of sources selected from the 2-Jy sample. Columns are (1) Source name, (2) date of observation, (3) ASKAP-BETA Scheduling Block ID (SBID), (4) duration of observations, (5) median spectral noise across the full band, (6) median fractional absorption noise (i.e. σ/S_{cont}).

Source	Date	SBID	t (hrs)	σ mJy/bm/ch	σ/S_{cont} (%)
<i>Band 1 observations: (711.5 - 1015.5 MHz)</i>					
PKS 0105–16	2015-sep-11	2538	4.5	43.3	0.68
	2015-sep-11	2541	4.5	58.0	0.86
	2015-dec-10	3302	2.5	33.6	1.02
	Total		7.0		0.47
PKS 0117–15	2015-jun-25	1998	6.5	35.5	0.53
	2015-sep-12	2546	3.0	57.5	0.72
	2015-dec-10	3302	2.5	36.3	0.47
	Total		12.0		0.31
PKS 0235–19	2014-sep-15	636	3.0	28.4	0.40
	2015-dec-10	3302	3.0	38.9	0.52
	Total		6.0		0.31
PKS 0252–71	2014-nov-11	1070	3.5	22.6	0.23
	2015-sep-12	2546	3.0	57.3	0.61
	2015-oct-01	2675	5.0	26.0	0.28
	2015-oct-02	2680	4.0	25.9	0.28
	2015-dec-12	3317	3.0	28.7	0.31
	2015-dec-13	3321	6.0	20.2	0.22
	Total		24.5		0.11
PKS 0409–75	2014-nov-20	1143	3.5	45.6	0.10
	2015-may-05	1753	4.0	20.7	0.11
	2015-aug-28	2483	3.0	29.2	0.15
	2015-sep-19	2591	5.0	24.6	0.11
	2015-sep-30	2668	5.0	22.2	0.11
	2015-oct-04	2687	6.0	21.6	0.10
	2016-feb-14	3577	7.0	23.5	0.13
Total		41.5		0.05	
PKS 1136–13	2014-nov-22	1147	2.0	34.0	0.50
	2014-nov-23	1150	2.0	32.5	0.48
	2015-dec-18	3394	3.0	29.8	0.49
	2016-jan-28	3469	4.0	51.2	0.80
	2016-jan-29	3470	4.0	47.8	0.81
	2016-feb-03	3500	3.0	55.8	0.87
	Total		18.0		0.25
PKS 1306–09	2014-nov-20	1143	3.5	54.9	0.60
	2015-jul-11	2093	3.0	50.7	0.61
	2015-oct-03	2681	4.0	26.8	0.49
	2015-dec-10	3303	3.5	33.3	0.52
	2015-dec-19	3399	3.5	30.4	0.51
	2016-jan-28	3469	7.0	51.0	0.87
	2016-jan-29	3470	5.0	42.7	0.79
	2016-jan-30	3475	6.0	42.5	0.78
Total		35.5		0.21	
PKS 1547–79	2014-nov-14	1096	3.0	23.6	0.51
	2016-jan-28	3469	5.0	42.1	0.88
	Total		10.5		0.44
PKS 1602+01	2015-jul-11	2093	4	43.8	0.51
	2015-dec-10	3308	4	29.0	0.43
	2015-dec-19	3399	3.5	30.0	0.42
	Total		11.5		0.26
PKS 1938–15	2015-jul-14	2127	3.0	32.9	0.31
	2015-sep-12	2546	3.0	43.7	0.44
	Total		6.0		0.41
PKS 2135–20	2016-jan-28	3468	2.5	67.1	1.26
	2016-jan-29	3472	2.0	68.7	1.31
	2016-jan-30	3480	3.0	57.4	1.11
	Total		7.5		0.69
<i>Band 2 observations: (967.5–1271.5 MHz)</i>					
PKS 0023–26	2015-nov-23	3184	3.0	50.1	0.50
PKS 0035–02	2015-nov-24	3190	4.0	94.9	1.68
PKS 0039–44	2015-nov-23	3185	3.0	84.8	1.68
PKS 1151–34	2015-nov-23	3182	3.0	66.4	0.97
PKS 2135–14	2015-nov-23	3184	3.0	52.1	3.10

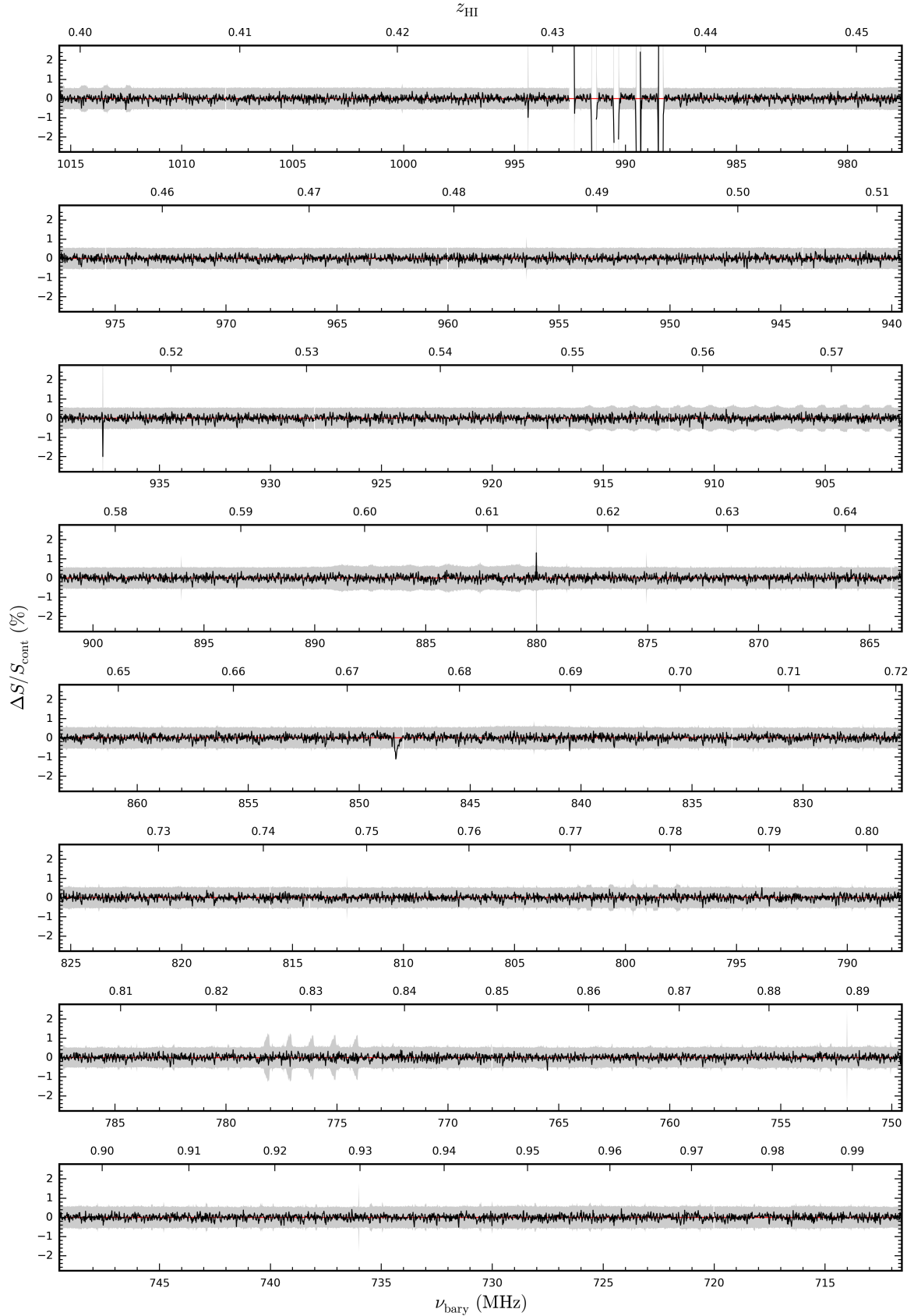


Figure B1. Full spectrum of a 5 hr observation of PKS 0409–75 observed on September 30, 2015. The grey band signals the 5σ noise level calculated from the rms of the image per channel. H I absorption is clearly detected at a frequency of 848 MHz. Some single channel noise peaks are seen occasionally (e.g. at 937.5 MHz) as well as artefacts due to correlator errors such as that seen around 990 MHz and 776 MHz.